Title
Estimating the impact of vadose zone heterogeneity on agricultural managed aquifer recharge: A combined experimental and modeling study

Authors
Zhou, Tiantian
Levintal, Elad
Brunetti, Giuseppe
et al.

Publication Date
2023-12-01

DOI
10.1016/j.watres.2023.120781

Estimating the impact of vadose zone heterogeneity on agricultural managed aquifer recharge: A combined experimental and modeling study

Tiantian Zhou[1], Elad Levintal[2], Giuseppe Brunetti[3], Spencer Jordan[1], Thomas Harter[1], Isaya Kisekka[1], Jiří Šimůnek[4], Helen E. Dahlke[1,*]

[1] Department of Land, Air and Water Resources, University of California, Davis, CA 95616, USA

[2] Zuckerberg Institute for Water Research, Blaustein Institutes for Desert Research, Ben-Gurion University of the Negev, Sde Boker campus, 84990, Israel

[3] Department of Civil Engineering, University of Calabria, Rende, Italy

[4] Department of Environmental Sciences, University of California, Riverside, CA 92521, United States

Corresponding author: E-mail address: hdahlke@ucdavis.edu (H.E. Dahlke).

Graphical Abstract

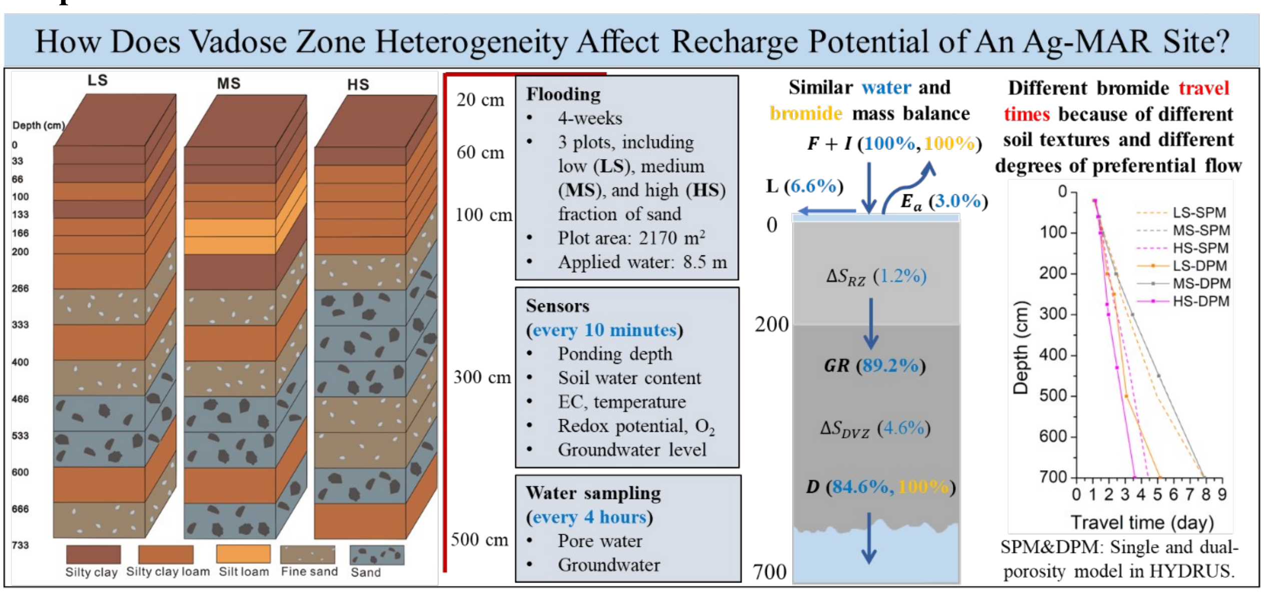

Abstract

Agricultural managed aquifer recharge (Ag-MAR) is a promising approach to replenish groundwater resources using flood water and cropland as spreading grounds. However, site selection, particularly the layering of sediment deposits in the subsurface, can greatly influence Ag-MAR efficacy as it controls water flow and solute transport in the vadose zone. In this study, we use the HYDRUS-1D software to simulate water flow and solute transport from the land surface to the groundwater table in three vadose zone profiles (LS, MS, HS) characterized by differing fractions of sand (44%, 47%, and 64%). For each profile, the single- and dual-porosity models (i.e., considering or not nonequilibrium water flow and solute transport) were calibrated using observed surface ponding, soil water content, and KBr breakthrough data. Water flow and bromide transport in the profile with the lowest sand fraction (LS) were best captured using the model that considered both preferential flow and nonequilibrium bromide transport. Water flow and bromide transport in the profile with the highest sand fraction (HS) was best simulated with the model that considered preferential flow and equilibrium bromide transport. Uniform water flow and nonequilibrium bromide transport provided the best fit for the third profile (MS). The degree of preferential flow was highest in the profile with the largest sand fraction (HS), which also showed the largest flow velocities compared to the profiles with lower sand amounts (LS and MS). Preferential flow did not significantly impact the overall water balance (within 3%), but caused a significant decrease in vadose zone travel times (bromide) by up to 38%, relative to a single-porosity model fit. Recharge efficiency varied between 88% and 90%, while the average travel times from the soil surface to groundwater varied up to 119% (from 3.6 to 7.9 days) between the three sites. This study demonstrates that similar recharge efficiency can be achieved at sites with differing soil texture profiles, but subsurface heterogeneity can substantially affect contaminant transport processes and their travel times.

Keywords: HYDRUS-1D, dual porosity model, preferential flow, subsurface runoff, bromide transport, travel time

1 Introduction

Groundwater contributes about 25% of irrigation water use, 50% of domestic water use, and 40% of industrial water use (Siebert et al., 2010; WWDR, 2022). In semi (arid) regions, groundwater withdrawal rates may exceed aquifer recharge rates, which causes groundwater depletion and associated environmental issues (Scanlon et al., 2012; Siebert et al., 2010) (Marwaha et al., 2021). Increasing groundwater recharge through managed aquifer management (MAR) is a promising approach for the sustainable development of groundwater resources (Sprenger et al., 2017; Wendt et al., 2021).

Agricultural managed aquifer recharge (Ag-MAR) is a fairly new practice that recharges groundwater by transferring excess surface water onto agricultural lands (Kocis and Dahlke, 2017). This practice can play a dual role in increasing agricultural water supply by replenishing groundwater and improving groundwater quality by diluting pollutant concentrations in groundwater (Bali et al., 2023). Ag-MAR is also less costly because it utilizes the existing irrigation infrastructure and farm fields as spreading sites without the additional construction of recharge basins or wells (Kourakos et al., 2019). Because of these advantages and vast agricultural lands available in many groundwater-dependent regions, a boom in Ag-MAR implementation has been witnessed in recent years, especially in the USA and Europe (Levintal et al., 2023b). However, there is uncertainty about how to identify suitable Ag-MAR locations that allow recharge of large water volumes but do not create additional environmental issues (Alam et al., 2021). One of the most problematic issues is the leaching of nitrate, salts, pesticides, and microbes from surface water or farmlands to groundwater (Bachand et al., 2014; Guo et al., 2023; Levintal et al., 2023a; Murphy et al., 2021; Waterhouse et al., 2020).

The prerequisite for addressing the above issues is an accurate understanding of water flow and solute transport processes in the vadose zone during Ag-MAR and their influencing factors. The influencing factors can be, in general, divided into three groups: a) hydrometeorological conditions, such as the intensity, amount, duration, and quality of precipitation or the applied water and the evaporation rate; b) hydrogeological conditions, including the vadose zone thickness, soil texture, and structure, soil chemical composition, and c) the type of land use and its management (Dahlke et al., 2018; Perzan et al., 2023; Siebert et al., 2010). Field experiments cannot always observe solute transport processes and groundwater contamination risks at the spatial-temporal scales at which they occur or might introduce the contaminant (Sasidharan et al., 2021; Wang et al., 2022; Wang et al., 2020). Numerical modeling can provide hydrologic information at a high spatial-temporal resolution, but the model calibration is often highly dependent on experimental data and is subject to the equifinality problem (Zhou et al., 2023). In contrast, field experiments combined with numerical models, such as HYDRUS, are more popular tools to investigate the impacts of different hydrometeorological and hydrogeological factors on groundwater recharge quantity and quality and associated crop root zone status. For example, Bali et al. (2023) used HYDRUS-2D to simulate the water balance of an alfalfa field in the San Joaquin Valley comparing different irrigation treatments in the summer (full and deficit irrigation) and winter flooding for groundwater recharge. Their results show that the fully irrigated alfalfa stand that was flooded in winter for groundwater recharge showed recharge efficiencies of 85%, 89% and 84% in 2020, 2021 and 2022, while those values were only 78%, 79% and 76% for the deficit irrigation treatment. Similarly, Ganot and Dahlke (2021) used HYDRUS-1D to validate an analytical solution-based root zone residence time model to develop guidance on the safe flooding duration for Ag-MAR for different soil textures (Ganot and Dahlke, 2021). Both studies estimated water balance components for different treatments/scenarios using a daily time step. However, to understand the effects of Ag-MAR on the fate and transport of solutes such as nitrate or salts, high-resolution (e.g., 10 minutes) data and numerical modeling are needed to fully quantify the complete recharge cycle of water and associated solutes from the soil surface through the vadose zone to the groundwater table.

In addition, preferential flow (a.k.a. nonequilibrium or nonuniform water flow in which the moisture front can propagate quickly to significant depths while bypassing a large part of the matrix pore-space) (Šimůnek et al., 2003) can lead to the earlier arrival of pathogens (Bradford et al., 2017), bacteria such as *Escherichia coli* (Arnaud et al., 2015), and other contaminants at the groundwater table. These adverse effects may pose a higher risk under Ag-MAR because of intensive applications of fertilizers and pesticides on agricultural lands. Preferential flow is often poorly characterized in field studies (Nimmo et al., 2021) and rarely considered in current numerical modeling analyses of Ag-MAR (Levintal et al., 2023b). Quantifying the degree of preferential flow and how it affects recharge and contaminants' transit times is one of the top priorities for selecting appropriate Ag-MAR sites.

In this study, we simulate water flow and solute transport in the vadose zone of three Ag-MAR plots in California at a temporal resolution of 10 minutes, using the HYDRUS-1D software, considering both single- and dual-porosity models. All three plots are located within the same 15 ha agricultural field, thus allowing the assessment of how within-field subsurface heterogeneity affects Ag-MAR vadose zone flow and transport processes. The specific objectives are to (1) identify and quantify to what degree preferential flow controls water flow and solute transport in the vadose zone under continuous ponded conditions, (2) quantify the flow of the recharge water, (3) estimate transit times of recharge water and contaminants from the land surface to the groundwater table using multiple indicators (bromide tracer, water table dynamics, soil and groundwater salt dynamics, and soil aeration dynamics), and (4) integrate hydrological and biogeochemical field and simulation data to assess Ag-MAR suitability.

2 Materials and Methods

2.1 Study Area

The Ag-MAR experiments were conducted in the source areas of three groundwater wells (LS, MS, HS) at a fallowed almond orchard west of Modesto, California (37º37"N, 121º05'W, Fig. 1). The area has a Mediterranean climate with mean annual precipitation of 330 mm, and potential evaporation of about 1356 mm (https://cimis.water.ca.gov/). Sediments in the vadose zone belong to the distal portions of the Tuolumne River alluvial fan, with channel sands as the base and heterogeneous floodplain sediments at the top. Groundwater flows from northeast to southwest (Fig. 1a) (Gurevich et al., 2021). The day before the flooding for Ag-MAR was started, groundwater table depths in the three wells were 6.34, 6.41, and 6.06 m, respectively. Therefore, we consider 7 m deep soil profiles in this study. While dominated by silty clay and silty clay loam, the profiles show progressively increasing fractions of sand from LS (44%), MS (47%) to HS (64%) (Fig. 2). The detailed soil particle distributions are shown in Table S1.

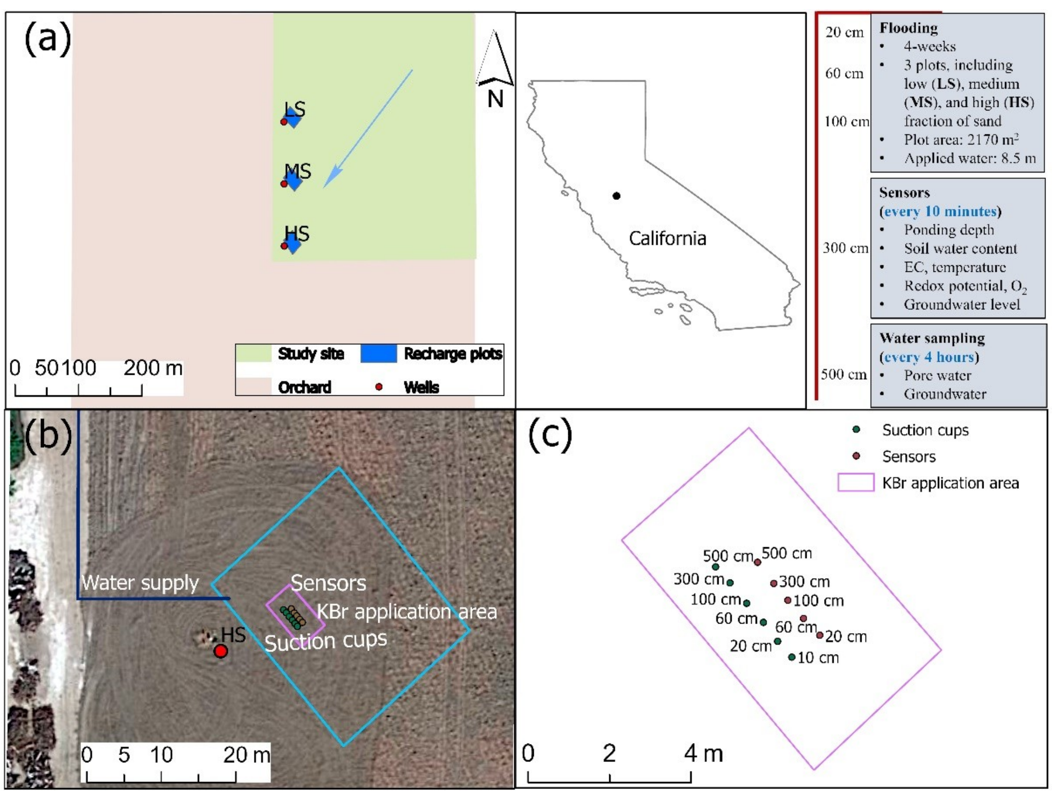

Figure 1. Location of the study site in California, USA. Locations of the three recharge plots upgradient of the three groundwater wells LS, MS and HS (a), of instrumentation and the potassium bromide (KBr) application site in each recharge plot (b), of sensors or suction cups at each sensor profile (c). The blue arrow in (a) shows the regional groundwater flow direction.

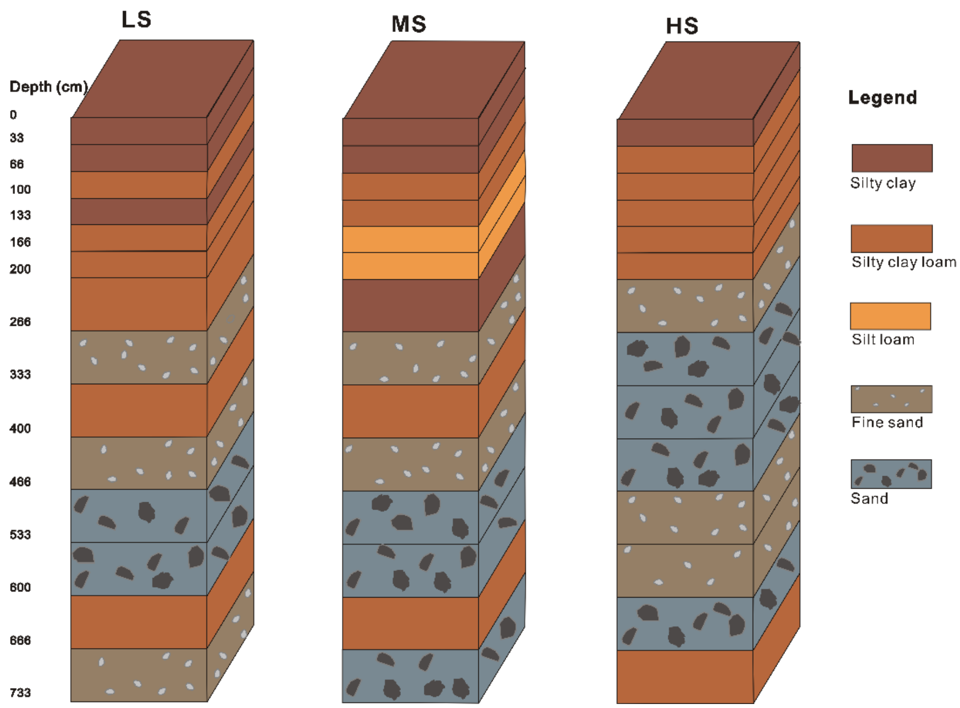

Figure. 2. Soil texture in the study profiles.

2.2 Field Monitoring and Data Collection

Recharge plots shown in Fig. 1a were bermed with native soil (0.5 m height, 1 m width). The field monitoring lasted from April 20 to June 14, 2022. The plots were flooded with surface water for 28 days, from May 3 (13:30) to May 31, 2022. Flooding was manually operated from May 3-5, 2022 to determine an irrigation schedule that would maintain a constant head (ponded water) on the field. During this period, the irrigation rate was considered continuous and constant. From 12:00 on May 6 to 8:00 on May 10, water was applied at all three sites for 2-hour intervals: 12:00-14:00, 18:00-20:00, 00:00-02:00, and 6:00-8:00. From 12:00 on May 10 to 7:40 on May 31, water applications were reduced to 100-minute intervals: 12:00-13:40, 18:00-19:40, 00:00-01:40, and 6:00-7:40. The flooding stopped at 9:00 on May 31, 2022. Totals of about 5,750 m^3, 6,281 m^3 and 5969 m^3 of water were applied within a flooding area of 694 m^2, 735 m^2, and 690 m^2 (i.e., 829.7, 855.8, and 866.3 cm in water depth) at LS, MS, and HS, respectively. Irrigation rates were calculated by dividing the total volume of applied water by the flooded surface area and the irrigation duration at corresponding stages (Table 1). As can be seen, between 5/6/2022 12:00 and 5/10/2022 11:43, water was applied at a higher rate. As a result, plots experienced a leak and some of the applied water spilled outside the berms overnight. Because the amount of water that spilled is unknown, a scaling factor was introduced to reduce the applied water amount on those days such that the simulated and observed ponding matched. As a result, scaled water application amounts reduced from 0.0850 to 0.0572 cm/min at LS, from 0.0820 to 0.0608 cm/min at MS, and from 0.0858 to 0.0613 cm/min at HS.

The bromide application area was about 7 m from each site's corresponding monitoring well (Fig. 1b). Br- was applied up-gradient to ensure it would move to the well area once it reached the groundwater. At each site, 4.833 kg of KBr (i.e., 3.245 kg of Br^-) was dissolved in approximately 100-110 gallons (380 L) of water and then applied over an area of 36.8 m^2 (i.e., 9.2 m* 4 m) for 20 minutes (starting at 14:00, 12:40, and 10:52 on May 2, 2022 in recharge plots LS, MS, and HS, respectively, i.e., one day before flooding) using a custom made drip irrigation system and a water tank. Br^- was thus applied at a concentration of 8164.18 ppm at an irrigation rate of 0.0540 cm/min.

Table 1. Irrigation schedule and rates.

LS	Flowmeter reading (m^3)	Flooding rate (cm/ min)	MS	Flowmeter reading (m^3)	Flooding rate (cm/ min)	HS	Flowmeter reading (m^3)	Flooding rate (cm/ min)
5/3/2022 13:30	0	0.0215	5/3/2022 13:30	0	0.0231	5/3/2022 13:30	0	0.0220
5/3/2022 17:06	117.8	0.0215	5/3/2022 17:01	99.0	0.0231	5/3/2022 16:58	108.0	0.0220
5/6/2022 12:00	708.5	0.0572	5/6/2022 12:00	805.2	0.0608	5/6/2022 12:00	683.1	0.0613
5/10/2022 11:43	1841.2	0.0675	5/10/2022 11:39	1962.9	0.0703	5/10/2022 11:52	1819.2	0.0716
5/26/2022 12:45	4839.3	0.0656	5/26/2022 12:36	5270.8	0.0687	5/26/2022 12:04	4981.1	0.0716
5/31/2022 7:40	5750.1	0	5/31/2022 7:40	6281.3	0	5/31/2022 7:40	5969.4	0

The meteorological data, including daily precipitation (P) and potential evaporation (E_p) (Fig. S1) were obtained from the CIMIS website (https://cimis.water.ca.gov/) from station 71 – Modesto, located 7 km west of the study site. The total potential evaporation during the monitoring period was 35.1 cm (Fig. S1).

The ponding level at the soil surface and the groundwater table depth were measured using pressure transducers (CS451, Campbell Scientific, UT, USA). Each recharge plot was instrumented with sensors at depths of 20, 60, 100, 250, and 500 cm at profile LS, 20, 60, 100, 300, and 450 cm at MS, and 20, 60, 100, 275, and 430 cm at HS) measuring soil water content, electrical conductivity (EC), soil temperature (TEROS12, Meter, WA, USA), O_2 (KE-25, Figaro, Japan), and oxidation-reduction potential (ORP) using constructed platinum electrodes. Hydrological (ponding level, soil moisture, soil temperature, groundwater table depth) and biogeochemical (O_2, ORP, EC) measurements were logged (using CR1000 and CR800, Campbell Scientific, UT, USA) at a 10-min time interval. Breakthrough curve data, monitoring the transport of the KBr tracer, were collected at minimum 4 hours using suction cups (LT-DBL, Irrometer, CA, USA) at the same depths as sensors.

The sensors or suction cups were installed along the long edge of the recharge plot, perpendicular to the groundwater flow direction (Fig. 1b). Each sensor or suction cup was about 0.5 m apart from the other to avoid interference. The distance between sensors and corresponding suction cups was about 1.12 m (Fig. 1c). The temporal distributions of relevant variables are shown in Figs. S1-S8.

2.3 HYDRUS-1D Model Setup

a. Initial and boundary conditions

Water flow and KBr transport in the unsaturated zone were simulated using the HYDRUS-1D software (Šimůnek et al., 2016). The 700-cm-thick soil profile was divided into five modeling layers, including 0-33 cm, 34-66 cm, 67-200 cm, 201-400 cm, and 401-700 cm, in which the third through the fifth modeling layers represent multiple physical soil layers (Fig. 2). The number of modeling layers was smaller than the number of physical layers because not all physical layers had a sensor collecting data. The simulation period was 55 days long, from April 20 to June 14, 2022, which included pre-flooding, flooding, and post-flooding periods. Since field water contents observations were limited to five depths, the simulation period was extended by considering a "spin-up" period (three months) before the flooding experiment. The spatial discretization resolution was 1 cm throughout the soil profile, while the temporal discretization resolution was variable, with a minimum time step of 0.01 minute.

The initial soil pressure head profile was first converted from measured water contents at five soil depths by using soil water retention curves of typical soil textures (Radcliffe and Šimůnek, 2018), and then linearly interpolated between any two measurement depths. The initial Br^- solute concentration was zero throughout the soil profile.

For water flow, the upper boundary condition (BC) was set to an atmospheric BC (with a maximum surface water layer of 50 cm, i.e., the height of the berms). In this BC, when the soil surface is not flooded, the potential water flux across the soil surface equals the difference between daily values of potential evaporation, E_0, and precipitation (P) or irrigation (I). When the soil surface is flooded, the boundary pressure head is equal to the water level at the surface, and the model calculates the infiltration flux. Depending on the soil moisture status, this atmospheric BC may appear as a Neumann BC (when the surface pressure head is within a critical range) or a Dirichlet BC (when the surface pressure head exceeds these critical values). The lower BC was set to a variable pressure head BC (i.e., Dirichlet BC), defined by the measured position of the groundwater table.

For solute transport, the upper BC was prescribed as a solute flux BC (i.e., a Cauchy BC), with bromide concentrations and irrigation fluxes during the bromide application as inputs. The model then automatically adjusts surface bromide concentrations depending on the thickness of the surface water level and evaporation/precipitation/irrigation fluxes and associated bromide concentrations. The lower BC was prescribed as a zero concentration gradient (i.e., a Neumann BC when only a convective solute flux occurs).

b. Single-porosity model (SPM)

Vapor flow can be neglected for conditions considered in this example. The one-dimensional uniform soil water movement in HYDRUS-1D can then be described using the Richards equation:

$$\frac{\partial \theta(h)}{\partial t}=\frac{\partial}{\partial z}\left[K(h)\left(\frac{\partial h}{\partial z}+1\right)\right] \quad (1)$$

where θ is the volumetric water content [L^3L^{-3}], t is time [T], h is the water pressure head [L], z is the spatial coordinate [L] (positive upward), and K is the hydraulic conductivity [LT^{-1}]. The soil water retention and hydraulic conductivity functions are described using the van Genuchten-Mualem (VGM) equations (Mualem, 1976; van Genuchten, 1980):

$$\theta(h)=\begin{cases}\theta_r+\dfrac{\theta_s-\theta_r}{\left[1+|\alpha h|^n\right]^m} & h<0\\ \theta_s & h \geq 0\end{cases} \quad (2)$$

$$K(h)=K_s S_e^l \text{¿} \quad (3)$$

$$S_e = \frac{\theta - \theta_r}{\theta_s - \theta_r} \tag{4}$$

$$m = 1 - 1/n \text{ (n>1)} \tag{5}$$

where θ_r and θ_s are the residual and saturated water contents [L^3L^{-3}], respectively; K_s is the saturated hydraulic conductivity [LT^{-1}]; S_e is the effective saturation [-]; l is the pore connectivity parameter (about 0.5); n is an empirical parameter related to the pore-size distribution [-], and α is an empirical parameter related to the inverse of the air-entry suction [L^{-1}].

The governing equation for solute transport is the advection-dispersion equation:

$$\frac{\partial \theta C}{\partial t} = \frac{\partial}{\partial z}\left(\theta D \frac{\partial C}{\partial z}\right) - \frac{\partial (qC)}{\partial z} \tag{6}$$

where C is the solute concentrations of soil water (ppm), q is the water flux [LT^{-1}], and D is the effective dispersion coefficient of solute in soil water [L^2T^{-1}] given by:

$$D = \lambda v + \frac{D_0 \tau}{\theta} \tag{7}$$

where λ is the soil dispersivity [L], v is the pore-water velocity [LT^{-1}], D_0 is the molecular diffusion coefficient [L^2T^{-1}], which is about 1.584 cm^2/d for Br^- (Isch et al., 2019; Köhne et al., 2004), and τ is the tortuosity factor [-].

c. Dual-porosity model (DPM)

The dual-porosity model divides the soil pore space into mobile and immobile regions. Water flow occurs only in the mobile region, described by the Richards equation, while water can also be stored but does not flowin the immobile region. The governing equations for water flow in the dual-porosity model are (Šimůnek et al., 2003):

$$\frac{\partial \theta_{mo}(h)}{\partial t} = \frac{\partial}{\partial z}\left[K(h)\left(\frac{\partial h}{\partial z} + 1\right)\right] - \Gamma_w \tag{8}$$

$$\frac{\partial \theta_{\Im}(h)}{\partial t} = \Gamma_w \tag{9}$$

where θ_{mo} and $\theta_{\Im}$ are water contents in the mobile and immobile regions [L^3L^{-3}], respectively. and Γ_w is the water transfer rate between the two regions [T^{-1}], which can be described as (Gerke and van Genuchten, 1993; Šimůnek et al., 2003):

$$\Gamma_w = \omega_w (S_{e,mo} - S_{e,\Im}) \tag{10}$$

where ω_w is the first-order rate coefficient for water transfer between the two regions [T^{-1}], and $S_{e,mo}$ and $S_{e,\Im}$ are effective saturations in the two regions [-], respectively. Compared with the single-porosity model, the dual-porosity model additionally considers three parameters, including the residual ($\theta_{\Im,r}$) and saturated ($\theta_{\Im,s}$) water contents in the immobile region, and ω_w. The other parameters are the same as in the single-porosity model and described by the VGM equations, except that now they are referred to as $\theta_{mo,r}$, $\theta_{mo,s}$, α, n, and K_s.

The dual-porosity model assumes that solute transport is limited to the mobile region, but there is a solute transfer between mobile and immobile regions. The governing equations for solute transport in the dual-porosity system are:

$$\frac{\partial(\theta_{mo} C_{mo})}{\partial t} = \frac{\partial}{\partial z}\left[\theta_{mo} D_{mo} \frac{\partial C_{mo}}{\partial z}\right] - \frac{\partial(q_{mo} C_{mo})}{\partial z} - \Gamma_s \qquad (11)$$

$$\frac{\partial(\theta_{\Im} C_{\Im})}{\partial t} = \Gamma_s \qquad (12)$$

$$\Gamma_s = \omega_s (C_{mo} - C_{\Im}) + \Gamma_w c^{¿} \qquad (13)$$

where D_{mo}, C_{mo}, and q_{mo} are the dispersion coefficient [L], solute concentration (ppm), and water flux [LT^{-1}] in the mobile region [L^{2}T^{-1}], respectively, $C_{\Im}$ is the solute concentration in the immobile region, Γ_s is the solute mass transfer between mobile and immobile regions [ML^{-3}T^{-1}], and ω_s is the solute mass transfer coefficient [T^{-1}]. $c^{¿}$ is the solute concentration that depends on the direction of mass transfer and equals C_{mo} for $\Gamma_w>0$ and $C_{\Im}$ for $\Gamma_w<0$. In this study, we consider three cases of the dual-porosity model (Fig. 3b, c, d).

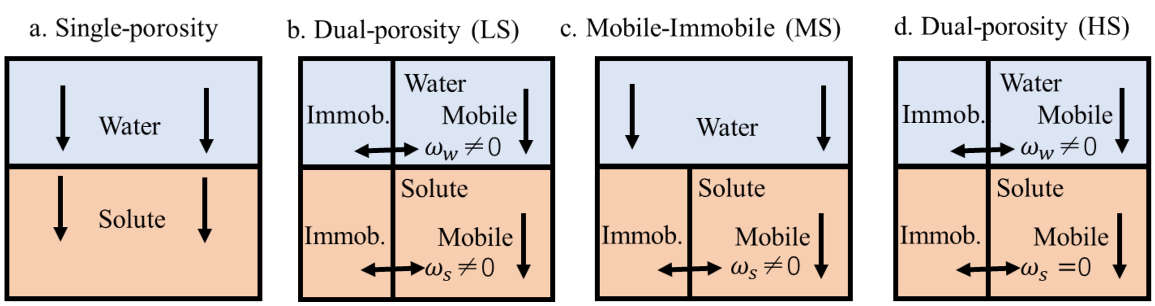

Figure 3. Conceptual schematics of different model setups (adapted from (Šimůnek and van Genuchten, 2008)).

2.4 Parameter estimation and model performance evaluation

The Levenberg-Marquardt algorithm in HYDRUS-1D was used to optimize soil hydraulic and solute transport parameters. This algorithm aims to minimize the sum of squared weighted deviations (SSQ_{total}) between observed and simulated surface ponding levels (SSQ_{sp}), soil water contents (SSQ_{wc}), and bromide concentrations in soil water (SSQ_{Br}) ($SSQ_{total} = SSQ_{wc} + SSQ_{sp} + SSQ_{Br}$). The square of the correlation coefficient (R^2), normalized-root-mean-square error (NRMSE), and Kling-Gupta efficiency (KGE) were calculated to evaluate the model performance. While the NRMSE index represents the average deviation of the residuals, R^2 measures the linear relationship between simulated and measured values, and KGE is a comprehensive indicator combining correlation and bias. The lower the SSQ and NRMSE, and the higher the R^2 and KGE, the better the fit between the simulated and observed values.

In this study, the dispersivity λ was not optimized since preliminary model runs indicated that the model performance was not sensitive to this parameter and only limited solute concentration data were available. The dispersivity was instead assumed to be equal to 70 cm, i.e., 1/10th of the total travel distance, representing a one-dimensional effective macrodispersivity (Gelhar et al., 1992).Soil hydraulic and other solute transport parameters were optimized using measured surface ponding levels, soil water contents, and bromide concentrations. During optimizations, parameters were adjusted layer by layer from top to bottom.

In the single-porosity model, the residual water contents were not optimized. Instead, the default values of corresponding soil textures were adopted first and then manually adjusted for the model to fit the measured data better. Therefore, four soil hydraulic parameters (θ_s, α, n, K_s) had to be optimized for each layer. The initial estimates of saturated water contents were manually set based on the steady water contents and common values for similar soil textures in Tables S2 (https://structx.com), while initial values of other parameters were obtained from the Rosetta module in HYDRUS-1D, based on measured average soil particle distribution data from this orchard (Table S1). The initial parameters for the soil layer with multiple soil textures were prescribed as those from the dominant soil texture.

To reduce the number of optimized parameters in the dual-porosity model, $\theta_{m,r}$ was set to zero, as done in many similar studies (Haws et al., 2005; Imig et al., 2023; Šimůnek et al., 2001). Therefore, eight soil hydraulic and solute transport parameters ($\theta_{mo,s}$, α, n, K_s, $\theta_{\Im,r}$,$\theta_{\Im,s}$, ω_w, ω_s) were optimized for each layer of profile LS (40 parameters in total), two soil hydraulic and solute transport parameters ($\theta_{\Im}$, ω_s) were optimized for each layer of profile MS (10 parameters in total), and seven soil hydraulic parameters ($\theta_{mo,s}$, α, n, K_s, $\theta_{\Im,r}$, $\theta_{\Im,s}$, ω_w) were optimized for each layer of profile HS (35 parameters in total). The previously optimized parameters of the single-porosity model were used as the initial values of parameters in the mobile zone of the dual-porosity model. For the immobile zone, the initial values $\theta_{\Im,r}$ were set the same as those in the single porosity model, while initial values of $\theta_{\Im,s}$ were prescribed as 0.1. The initial values of ω_w, ω_s were obtained from the literature (Imig et al., 2023; Isch et al., 2019; Köhne et al., 2004).

The correlation matrices for each scenario were calculated using the Jacobian approximation of the Hessian matrices around the optima (Šimůnek and Hopmans, 2002). This enabled us to detect and discuss parameters' interaction and test the appropriateness of applying the single or dual-porosity models.

3 Results

3.1 Single-Porosity Model: Parameters and Performance

The optimized parameters for the single-porosity model are shown in Table 2. The soil retention and hydraulic conductivity curves for optimized parameters are shown in Fig. S9. Overall, the optimized parameters were within typical values from literatures findings (Text S1). The exceptions are that the saturated hydraulic conductivities (0.027-0.034 cm/min) for the silty clay layers (0~66 cm) were far higher than the typical values (0.0062 cm/min in Table S4) according to (Clapp and Hornberger, 1978; Li et al., 1976). The saturated water contents for the silty clay loam and silt loam layers (67~200 cm) were 0.21-0.29 cm^3/cm^3, below typical values of 0.29-0.52 cm^3/cm^3 for these textural classes, according to Table S2.

The model performance is shown in Table 4 and Figs. 4-6. Overall, the simulated values and trends of surface ponding levels, soil water contents, and bromide concentrations matched the observations well when SPM was used. The observed surface ponding levels quickly increased to their maximum (about 13 cm, 17 cm, and 13 cm for profiles LS, MS, and HS, respectively) because of intense and continuous irrigation at the beginning of the experiment. After that, the ponding level decreased and remained relatively stable as irrigation became intermittent (about every 4 hours) and potential evaporation increased (Fig. S1).

The water contents at all depths exhibited increasing trends during the flooding period and decreased during the post-flooding period. Simulated wetting fronts arrived later than those observed as depth increased, especially at LS. The bromide concentrations at all depths first increased and then decreased with time. Similarly to wetting fronts, simulated early breakthroughs at Profiles LS and HS arrived later than those observed as depth increased.

At LS, simulated breakthrough curves (BTCs) at the bottom (250 and 500 cm) showed a slower response to flooding than those observed. In addition, the observed BTCs had much more significant tailings than those simulated. Observed BTCs also displayed secondary peaks at 100 and 250 cm. At HS, simulated BTCs always occurred slightly later than those observed, except at depths of 10, 20, and 275 cm. At MS, the arrival of the simulated BTCs matched well with those observed. However, the model could not capture strong tailings at 300 and 450 cm depths.

3.2 Dual-Porosity Model: Parameters and Performance

As discussed in Section 3.1, in profile MS, arrival times of the simulated wetting and bromide fronts at depths of 300 and 450 cm matched very well those observed, but simulated bromide leaching was faster than observed when SPM was used (i.e., strong tailing of observed BTCs). Therefore, the special case of the dual-porosity model, i.e., the mobile-immobile model (MIM), was used. This model assumes that water flow is uniform (i.e., no preferential flow), the immobile water content is constant, water mass transfer between the two regions is zero, and solute is transported between the mobile and immobile regions by diffusive exchange (Isch et al., 2019; Köhne et al., 2004). In other words, the water transfer coefficient, ω_w, was equal to zero, while ω_s was optimized (Fig. 3b).

In profile HS, no significant tailing was observed in the bromide BTCs, and arrival times of bromide fronts simulated using SPM were retarded compared to those observed. Thus, it was assumed that the earlier arrival of observed bromide fronts compared to those simulated was caused only by nonuniform (preferential) water flow (Haws et al., 2005). In this case, ω_s was set to zero while ω_w was optimized (Fig. 3c).

In profile LS, significant tailing was observed in the bromide BTCs, and the arrival of bromide fronts simulated using SPM was retarded compared to those observed. The observed BTCs also displayed secondary peaks at 100 and 250 cm. In this case, bromide tailing was likely caused by diffusive mass transfer between mobile and immobile regions and the fast bromide front arrival by nonuniform (preferential) water flow (Isch et al., 2019; Köhne et al., 2004), and therefore, both ω_w and ω_s were optimized (Fig. 3d).

The optimized parameters for the three dual-porosity models are shown in Table 3. The model performance is shown in Table 4 and Figs. 4-6. DPM provided a slightly better fit to the observed data than SPM. Notably, the use of the dual-porosity model (considering nonequilibrium water flow and solute transport) resulted in a slight decrease in NRMSEs and similar correlation coefficients (R^2) for simulated and observed BTCs at profiles LS and MS (Table 4). Although using the dual-porosity model increased R^2, it also increased NRMSEs for BTCs at Profile HS. The cumulative water and bromide transfer from the mobile to immobile zone ($Cum\Gamma_w$ and $Cum\,\Gamma_w$, a higher value means higher degree of nonequilibrium flow and solute transport) are shown in Fig. S16. Therefore, Profile HS showed a higher propensity for preferential flow than LS, while MS showed the least indication of preferential flow.

The correlation matrices for parameters of different models are shown in Fig. S10-S15. When considering only the strong correlations (R>0.6), only α_3-α_4, K_{s1}-K_{s3} were negatively correlated when using SPM at LS, while many more parameters were positively and negatively correlated when using DPM. This suggests that DPM improved model performance due to over-parameterization. However, both SPM and DPM structures could not capture the observed bromide BTCs well (Table 4). At MS, both SPM and DPM showed a positive correlation between K_{s3}-α_1 and negative correlations between K_{s1}-α_1, K_{s1}-α_2, K_{s5}-α_2, K_{s3}-K_{s1}. Both SPM and DPM performed well and similarly. This indicates that SPM and DPM structures were equivalent and sufficient in describing the observations, and it was unnecessary to apply DPM at MS. At HS, for SPM, n_1-α_3, K_{s3}-α_3, K_{s3}-α_4 were positively correlated, while α_2-$\theta_{s,4}$, α_4-α_2, K_{s1}-α_3, K_{s3}-K_{s2}, K_{s1}-n_1, K_{s2}-α_4 were negatively correlated. For DPM, only four parameter pairs were correlated, including K_{s1}-α_1 (positive), and n_1-$\theta_{s,1}$, K_{s3}-K_{s2}, ω_{w3}-$\theta_{\Im,r5}$ (negative), and model performance improved a little compared to SPM. This emphasizes the necessity of employing DPM at HS.

Table 2. Optimized parameters of the single-porosity model.

Site	Depth (cm)	θ_r (cm^3/cm^3)	θ_s (cm^3/cm^3)	α (cm^{-1})	n (-)	K_s (cm/min)
	0-33	0.105	0.374	0.016	1.747	0.031
	34-66	0.115	0.301	0.012	1.305	0.029
LS	67-200	0.125	0.291	0.007	1.215	0.015
	201-400	0.045	0.230	0.013	3.800	9.000
	401-700	0.151	0.528	0.061	2.000	0.200
MS	0-33	0.105	0.374	0.009	1.831	0.028
	34-66	0.080	0.284	0.010	1.468	0.027
	67-200	0.095	0.210	0.006	1.598	0.015
	201-400	0.085	0.329	0.003	1.084	0.417

	401-700	0.091	0.428	0.088	3.235	0.030
HS	0-33	0.050	0.305	0.011	1.232	0.034
	34-66	0.105	0.284	0.009	1.276	0.017
	67-200	0.080	0.241	0.006	1.300	0.017
	201-400	0.025	0.210	0.013	2.943	6.000
	401-700	0.040	0.210	0.061	3.099	2.000

Table 3. Optimized parameters of the dual-porosity model.

Site	Depth (cm)	$\theta_{mo,r}$ (cm³/cm³)	$\theta_{mo,s}$ (cm³/cm³)	α (cm⁻¹)	n (-)	K_s (cm/min)	$\theta_{\Im,r}$ (cm³/cm³)	$\theta_{\Im,s}$ (cm³/cm³)	ω_w (min⁻¹)	$\theta_{\Im}$ (cm³/cm³)	ω_s (min⁻¹)
LS	0~33	0	0.254	0.012	1.487	0.033	0.077	0.100	4.100E-08		1.052E-03
	34~66	0	0.181	0.012	1.303	0.029	0.115	0.130	3.270E-07		6.458E-03
	67~200	0	0.176	0.007	1.231	0.015	0.112	0.130	5.870E-07		1.276E-05
	201~400	0	0.103	0.014	3.096	16.033	0.048	0.110	5.870E-07		2.890E-04
	401~700	0	0.228	0.061	2.100	0.050	0.150	0.450	2.670E-08		4.614E-06
MS	0~33	0.105	0.374	0.009	1.831	0.028				6.116E-02	7.000E-03
	34~66	0.080	0.284	0.010	1.468	0.027				5.359E-02	7.000E-03
	67~200	0.095	0.210	0.006	1.598	0.015				2.710E-03	4.616E-03
	201~400	0.085	0.329	0.003	1.084	0.417				5.271E-02	1.318E-03
	401~700	0.091	0.428	0.088	3.235	0.030				8.007E-02	3.528E-03
HS	0~33	0	0.205	0.011	1.207	0.035	0.031	0.100	6.082E-04		
	34~66	0	0.134	0.008	1.324	0.017	0.100	0.150	2.978E-04		
	67~200	0	0.134	0.006	1.473	0.016	0.091	0.100	5.291E-03		
	201~400	0	0.160	0.014	2.956	6.515	0.030	0.050	3.633E-03		
	401~700	0	0.110	0.067	2.849	2.077	0.036	0.100	6.877E-03		

Table 4. The performance of the single-porosity model [SPM] and dual-porosity model [DPM] to simulate surface ponding levels, soil water contents, and bromide concentrations for the three soil profiles (LS, MS, HS).

Simulated variable	Indicator	LS		MS		HS	
		SPM	DPM	SPM	DPM	SPM	DPM
Surface ponding level	R^2	0.435	0.460	0.624	0.624	0.632	0.634
	NRMSE	0.276	0.263	0.287	0.287	0.279	0.248
	KGE	0.545	0.544	0.656	0.656	0.334	0.337
Water content	R^2	0.852	0.873	0.764	0.764	0.908	0.907
	NRMSE	0.201	0.190	0.220	0.220	0.181	0.185
	KGE	0.913	0.903	0.849	0.849	0.939	0.935
Bromide concentration	R^2	0.238	0.237	0.569	0.569	0.646	0.791
	NRMSE	1.150	1.139	1.406	1.393	1.856	1.933
	KGE	-0.046	0.047	0.446	0.458	0.412	0.592

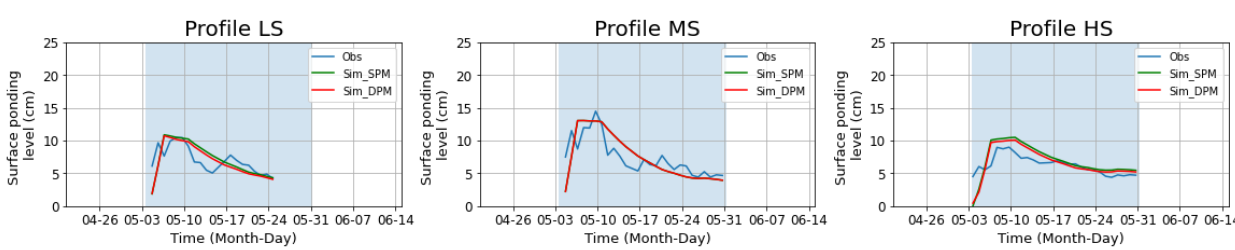

Figure 4. Observed and simulated (using the single-porosity model [SPM] and dual-porosity model [DPM]) surface ponding water levels for the three soil profiles. The blue shaded area indicates the flooding period.

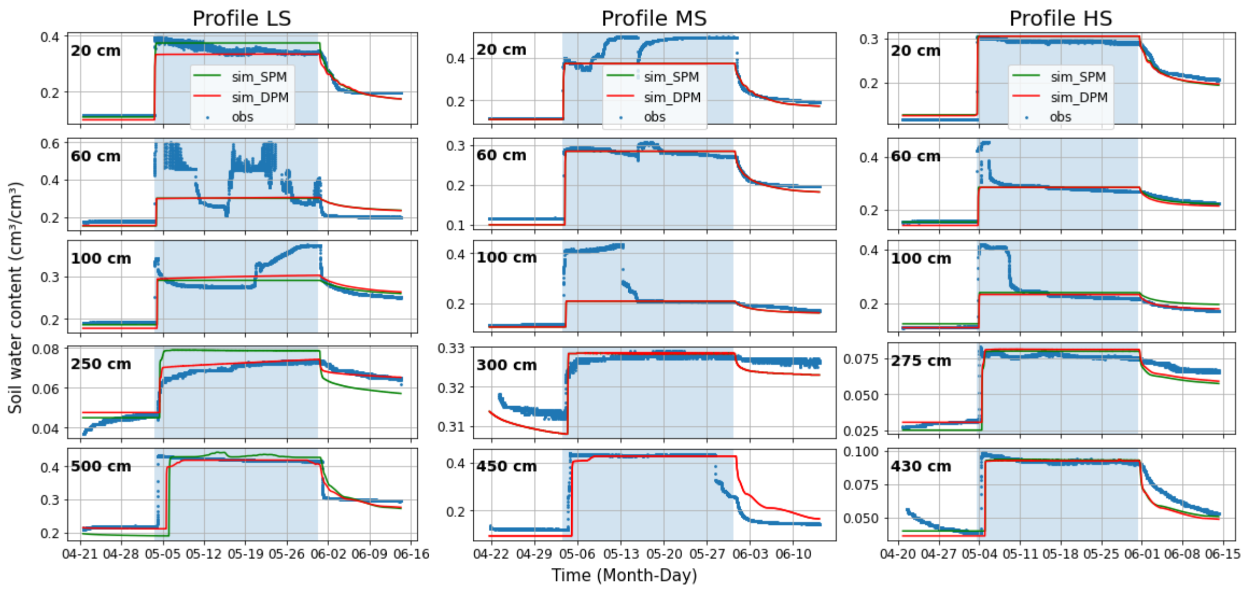

Figure 5. Observed and simulated (using the single-porosity model [SPM] and dual-porosity model [DPM]) soil water contents at different depths for the three soil profiles (LS, MS, HS).

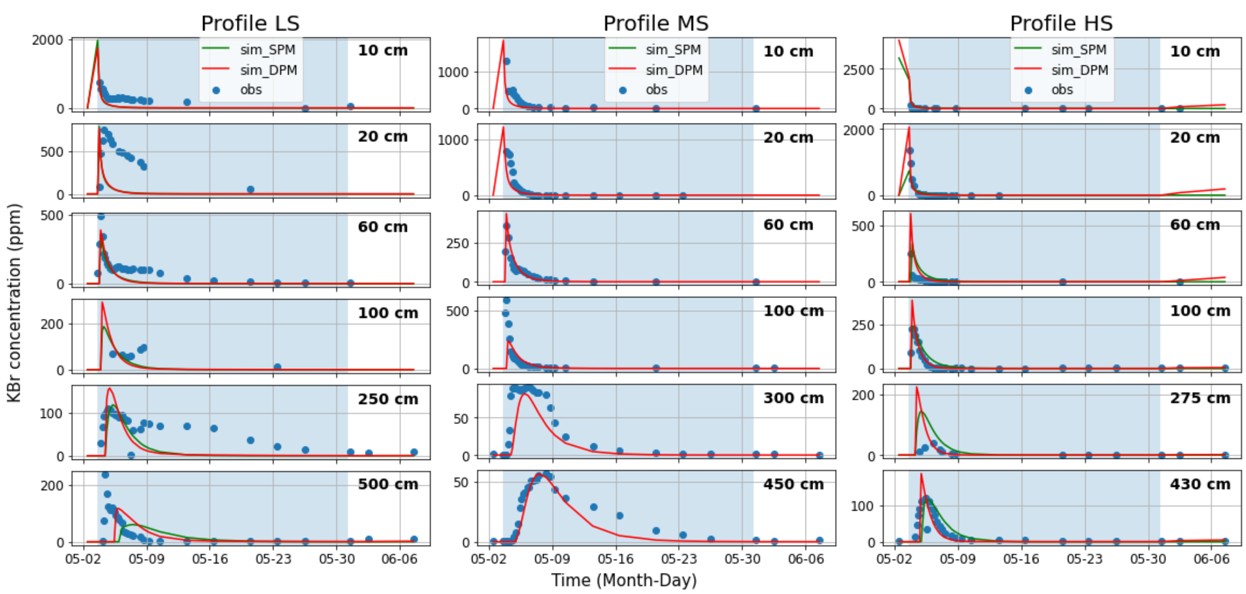

Figure 6. Observed and simulated (using the single-porosity model [SPM] and dual-porosity model [DPM]) bromide concentrations at different depths for the three soil profiles (LS, MS, HS).

3.3 Water Mass Balance

The water balance calculation results obtained using the single- and dual-porosity models were very similar (differences were within 2%), as shown in Table 5 and Fig. 7b. Regarding the amount of groundwater recharge as a fraction of the total surface water applied (a.k.a. recharge efficiency, calculated as (D+ΔS_{DVZ})/(P+I)), profile HS yielded the largest recharge, LS the smallest, while MS ranked between the two. All three profiles showed a similar groundwater recharge efficiency (88%-90%). Overall differences in mass balance components between the three profiles were not very large (within 3%).

This is because the top three layers (0~200 cm) of all three soil profiles quickly reached saturation during intensive Ag-MAR (Fig. 5, Table 2). In such a case, evaporation from the soil surface was close to potential evaporation and thus was similar between different sites. Water movement from the soil surface to the bottom of the third layer was only driven by the ponding and gravity gradients. According to Darcy's law, soil drainage rates below 200 cm (equivalent to groundwater recharge since we included soil water storage in the deep vadose zone into groundwater recharge as well) can be calculated as:

$$GR=\frac{-K_{sTop,eff}*(L_{Top}+SP)}{L_{Top}} \tag{14}$$

where L_{Top} is the total thickness of the top three soil layers (200 cm), SP is the surface ponding depth, $K_{sTop,eff}$ is the effective saturated hydraulic conductivity of the top three layers as follows:

$$K_{sTop,eff}=\frac{\sum_{j=1}^{3} L_j}{\sum_{j=1}^{3} \frac{L_j}{K_{s,j}}} \tag{15}$$

where L_j and $K_{s,j}$ are the thickness and the saturated hydraulic conductivity of each layer (Tables 2~3), respectively.

At LS, MS, and HS, the $K_{sTop,eff}$ values were calculated as 0.018, 0.018, and 0.019 cm/min for SPM, and 0.018 cm/min for DPM. The corresponding mean ponding depths measured during Ag-MAR were 6.29, 7.72, and 7.14 cm. The groundwater recharge rates were thus estimated to be 0.019, 0.019, and 0.020 cm/min for SPM and 0.019 cm/min for DPM. In other words, groundwater recharge was determined by (and close to) $K_{s\,\mathrm{Top,eff}}$, because gravity gradients prevailed over the ponding gradients. These values were also consistent with water fluxes at 200 cm (0.018, 0.019, and 0.020 cm/min at LS, MS, and HS, respectively for both SPM and DPM) simulated by HYDRUS-1D (Fig. S17), validating their accuracy. Therefore, the soil water balance was similar between the three soil profiles.

Table 5. Water balance components for different soil profiles.

Term	LS					MS					HS				
	SPM		DPM		Relative difference	SPM		DPM		Relative difference	SPM		DPM		Relative difference
	cm	%	cm	%	%	cm	%	cm	%	%	cm	%	cm	%	%
P+F	829.7		829.7			855.8		855.8			866.3		866.3		
L	63.9	7.7	63.9	7.7	0	51.5	6.0	51.5	6.0	0	53.0	6.1	53.0	6.1	0
R	0	0	0	0	0	0	0	0	0	0	0.0	0	0	0	0
E	23.9	2.9	24.9	3.0	0.1	24.7	2.9	24.7	2.9	0	24.4	2.8	24.3	2.8	0
D	687.1	82.8	693.2	83.5	0.7	729.5	85.2	729.5	85.2	0	738.2	85.2	739.3	85.3	0.1
ΔS_R	10.7	1.3	11.8	1.4	0.0	20.3	2.4	9.1	1.1	-1.3	10.0	1.2	10.1	1.2	0
ΔS_D	43.8	5.3	35.7	4.3	-1.0	28.7	3.4	39.9	4.7	1.3	42.6	4.9	42.2	4.9	0
GR	730.9	88.1	728.9	87.9	-0.2	758.2	88.6	769.4	89.9	1.3	780.8	90.1	781.5	90.2	0.1

P: precipitation, F: flood irrigation, L: water loss outside the berms, R: runoff, E: evaporation, D: drainage, ΔS: storage change in the root zone 0~150 cm (ΔS_{RZ}) and deep vadose zone (ΔS_{DVZ}¿, GR: groundwater recharge including D and ΔS_{DVZ} because water flow is considered to be one-dimensional and thus deep drainage below the root zone will eventually recharge groundwater with a delay (de Vries and Simmers, 2002).

3.4 Bromide Travel Time

The peak displacement method estimates travel times from the time lag between peaks in the measured input (irrigation water) and output (soil water at different depths) bromide BTCs (Zhou et al., 2021). The travel times and average velocities of bromide front from the soil surface to different soil depths calculated with the peak displacement method are shown in Table 6. In general, the mean velocities of bromide front increased as depth increased for both the single- and dual-porosity models. Due to preferential flow, the travel times of bromide front from the soil surface to different depths of the soil profiles decreased by up to 38%, while the transport velocities increased by up to 61%, compared to the single-porosity model. Overall, travel times (flow velocities) were longest (slowest) at MS, followed by LS, and shortest (fastest) at HS. The travel times from land surface to groundwater table varied from 3.6 to 7.9 days, resulting in an overall average transport velocity difference between the three sites of up to 119%. Travel times and transport velocities inferred from water table dynamics, soil aeration, and soil and groundwater salt leaching were also analyzed (Texts S2~S4), which were overall comparable to those in Table 6.

Darcy's law calculates water fluxes through the entire cross-sectional area, but water flow occurs only in soil pores. Therefore, the pore water velocity v (or bromide front velocity when considering only convective bromide transport) is related to Darcy flux J_w by soil water content θ (Radcliffe and Šimůnek, 2018):

$$v = J_w / \theta \tag{16}$$

During Ag-MAR, the thickness-weighted water contents at the top three layers θ_{Top} were 0.303, 0.248, and 0.261 cm^3/cm^3 at LS, MS, and HS, respectively. The bromide front velocities at 200 cm $v_{200\,cm}$ were 78.43, 81.30, and 85.84 cm/day for SPM, and 105.26, 81.97, and 105.26 cm/day for DPM at LS, MS, and HS, respectively (Table 6). The corresponding Darcy fluxes for groundwater recharge GR calculated using Eq. 16 were therefore 0.017, 0.014, and 0.016 cm/min for SPM, and 0.022, 0.014, and 0.019 cm/min for DPM at LS, MS, and HS, respectively. These values were overall consistent with those in Section 3.3, despite some differences probably due to dispersive or diffusive bromide transport in this study.

Table 6. Travel times and average velocities of bromide front from the soil surface to different soil depths.

Term	Depth (cm)	LS SPM	LS DPM	LS Relative difference %	MS SPM	MS DPM	MS Relative difference %	HS SPM	HS DPM	HS Relative difference %
Travel time (day)	20	1.09	1.08	-0.9	1.12	1.12	0.0	1.19	1.17	-1.7
	60	1.38	1.38	0.0	1.42	1.42	0.0	1.37	1.33	-2.9
	100	1.69	1.51	-10.7	1.61	1.62	0.6	1.57	1.47	-6.4
	200	2.55	1.90	-25.5	2.46	2.44	-0.8	2.33	1.90	-18.5
	250 (300, 275)	2.71	2.33	-14.0	3.46	3.46	0.0	2.52	1.97	-21.8
	500 (450, 430)	4.97	3.09	-37.8	5.10	5.08	-0.4	3.23	2.50	-22.6
	700	7.86	5.17	-34.2	7.91	7.90	-0.1	4.43	3.60	-18.7
Bromide front velocity (cm/day)	20	18.35	18.52	0.9	17.86	17.86	0.0	16.81	17.09	1.7
	60	43.48	43.48	0.0	42.25	42.25	0.0	43.80	45.11	3.0
	100	59.17	66.23	11.9	62.11	61.73	-0.6	63.69	68.03	6.8
	200	78.43	105.26	34.2	81.30	81.97	0.8	85.84	105.26	22.6
	250 (300, 275)	92.25	107.30	16.3	86.71	86.71	0.0	109.13	139.59	27.9
	500 (450, 430)	100.60	161.81	60.8	88.24	88.58	0.4	133.13	172.00	29.2
	700	89.06	135.40	52.0	88.50	88.61	0.1	158.01	194.44	23.1

4 Discussion

4.1 Impact of preferential flow on model performance

The lag between observed and simulated wetting and/or bromide fronts in the deeper profiles of LS and HS when using the single porosity model (Figs. 5-6) clearly indicates the existence of preferential flow. Preferential flow likely occurred due to the combined effects of intense infiltration, dry climate (initially dry soil), soil texture heterogeneity, presence of macrofauna (e.g., earthworms), and active and decaying crop roots. Continuous water ponding at the soil surface resulting from the application of about 8-9 m of water in a month (Table 1) is more likely to produce preferential flow than intermittent flooding from natural precipitation (Chen et al., 2002; Mitchell and van Genuchten, 1993; Selker et al., 1995). The semi-arid climate and particularly the rain-free summer likely promoted the formation of macropores, especially in the top soil, which had a higher clay content and is therefore more prone to shrink-swell dynamics that can create desiccation cracks (Jiang et al., 2010). In addition, the almond orchard was just fallowed, with almond wood chips incorporated into the soil to about 50 cm resulting in higher hydraulic conductivities during the experimental period (Fig. 7a(1)). Research has shown that the infiltration rate may increase in soils with decaying plant roots or with wormholes serving as preferential flow paths (Fig. 7a(3) and 7a(4)) (Mitchell et al., 1995). Such features could explain preferential flow in the top 0-66 cm of LS and HS (Fig. 2). The presence of a coarser-textured soil layer (near the bottom of the profiles) overlain by a fine-textured soil layer may produce funnel or fingered flow (Fig. 7a(5) and 7a(6)) (Council, 2001; Wang et al., 2018), resulting in preferential flow in the deep layers of profile LS and HS (Figs. 5-6).

There were only small differences between the single- and dual-porosity models in the simulated surface ponding levels and soil water contents (see the model performances in Table 4). However, the dual-porosity model (considering preferential flow) produced much better fits for the bromide BTC values and trends observed at LS (Fig. 6). However, both SPM and DPM could not capture the observed bromide BTCs very well (Table 4). This may be associated with observation errors since the bromide samples were not taken at the exact same locations as the soil sensors (at a horizontal distance of 1.12 m). It might also indicate that some other hydrological processes may be occurring that cannot be described by SPM and DPM (discussed in Section 4.2). At HS, the dual-porosity model captured overall trends better (increased R^2), but it did not capture observed values (increased NRMSEs) as well as the single porosity model. The dual-porosity model simulated much higher peak values of the bromide BTCs than were observed at HS. This may be related to the fact that the temporal resolution of the bromide samples taken in the field was at minimum 4 hours and hence may not have accurately captured the real peak values that the dual-porosity model suggested. Finer spatial and temporal resolutions of field measurements would better constrain model parameters and improve model performance.

4.2 Impacts of flow dimensionality on model performance

Measured soil water contents showed abrupt decreases (before May 16) and/or increases (after May 16) in all three profiles at depths of 60 and 100 cm that cannot be captured by the model (Fig. 5). There was also strong tailing in measured BTCs at shallow depths of LS (Fig. 6), indicating significant initial tracer storage and slow re-release at these shallow depths. In addition, measured steady water contents at layers below 200 cm were very low, e.g., about 0.1 cm^3/cm^3 at 250 cm of LS, and about 0.1 cm^3/cm^3 at 275 and 430 cm of HS, far smaller than their saturated water contents (Table 2). The O_2 concentrations at these depths were still high during flooding (Fig. S5a, S6a, S7a), indicating the soil was mostly unsaturated at those depths.

As shown in Tables 2-3, all three profiles had a low conductivity layer (silty clay or silty clay loam, as shown in Fig. 2) at 67-200 cm depth (Ks=0.015-0.017 cm/min) followed by a higher conductivity layer (Ks=0.4-16 cm/min in LS, HS) at 201-400 cm depth. This lithological combination may form the capillary barrier, where water flux to the deeper profiles was limited and likely only occurred as finger flow, while lateral flow within the low-conductivity layers (i.e., interflow H_2 in Fig. 7) likely dominated (Ho and Webb, 1998). As a result, water and solutes could have been perched at these less permeable layers, allowing less water and solutes to move downwards to deeper layers until a critical soil water potential is reached (Si et al., 2011), explaining the low, unsaturated water contents at soil depths below 200 cm. This phenomenon was also studied and discussed in previous studies. For example, (Botros et al., 2012; Harter and Yeh, 1996) demonstrated the lateral spreading of solutes due to the heterogeneous unsaturated zone leads to extensive tailing in the observed breakthrough curves.

The three profiles had almond wood chips incorporated into the top soil layer, following removal of a 20-year-old orchard, creating flow pathways with much higher soil hydraulic conductivities within the top 30 cm (Fig. 7a(1)). This is likely the reason that estimated soil hydraulic conductivities for the silty clay layers were higher than their typical representative values (Tables 2-3 and Text S1). This much higher saturated hydraulic conductivity of the top soil layer, compared to the underlying clay soils, likely promoted lateral water flow (i.e., interflow H_1 in Fig. 7a). The relatively lower-than-expected saturated water content of third layer, which may be the outcome of compaction from agricultural operations, further contributes to increased lateral flow within the top soil layers.

Owing to the occurrence of lateral flow, the wetted unsaturated zone is likely broader than the size of the ponding basins. In the 1D effective parameter model representation of this system, the effective, fitted saturated water content for the silty clay loam/silt loam layer at 67~200 cm (discussed in Text S1) is therefore lower than their typical values (Text S1). The fitted, high effective saturated hydraulic conductivities (about 0.4-16 cm/min) at 201~400 cm (Tables 2-3) allow for the speed up of this excess downward water flow, which resulted in a better fit in water contents at these depths, but it also promoted bromide leaching and thus caused lower simulated bromide concentrations than observed at the deeper depths (e.g., 250 and 500 cm of LS; 300 and 450 cm of MS, Fig. 6). Based on the analysis above, the conceptual models of water flow and bromide transport in the three profiles can be deduced (Fig. 7a).

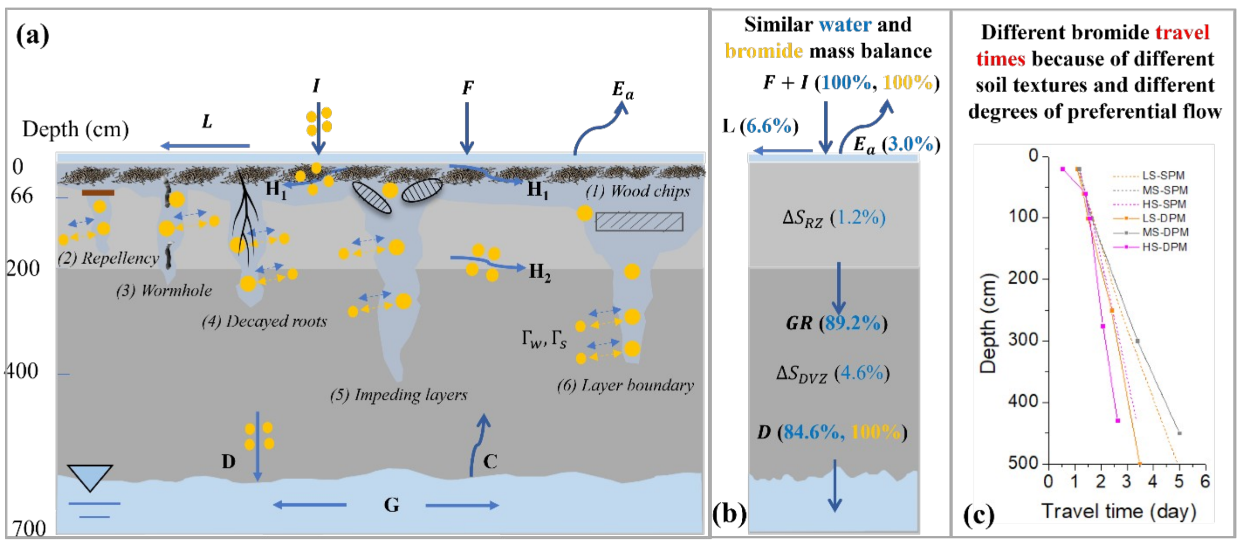

Figure 7. Conceptual models of water flow and bromide transport (a), water and bromide mass balance (b), and bromide travel times (c) during Ag-MAR in the study profiles. Blue polygons and orange circles represent water and bromide molecules, respectively. Blue and orange arrows represent water flow and bromide transport directions, respectively. I: Bromide application; F: Flooding; L: Water loss outside the berms; E_a: Evaporation; H_1: Horizontal flow through wood chips; H_2: horizontal flow caused by capillary barrier; D: Deep drainage; C: Capillary rise; G: Groundwater flow. (1)~(6) are possible preferential flow mechanisms caused by (1) wood chips, (2) soil repellency, (3) wormhole, (4) decayed roots, (5) impeding layers, and (6) layer boundaries. Γ_w and Γ_s represent the water and solute transfer terms in Eqs. 10 and 13, respectively. In this study, $\Gamma_w \neq 0$, and $\Gamma_s \neq 0$ at LS (preferential flow and nonequilibrium bromide transport); $\Gamma_w \neq 0$, and Γ_s=0 at HS (preferential flow and equilibrium bromide transport); $\Gamma_w = 0$, and $\Gamma_s \neq 0$ at MS (uniform water flow and nonequilibrium bromide transport). SPM and DPM represent single and dual-porosity model in HYDRUS, respectively.

4.3 Other possible reasons behind model deficiencies

First, as discussed in Section 4.2, there were abrupt decreases in water contents at 60 and 100 cm at LS, at 100 cm at MS, and at 60 and 100 cm at HS at the beginning of the flooding (before May 17) that could not be captured by the model (Fig. 5). This could be due to some subsurface heterogeneities (discussed in Section 4.2) or measurement errors such as overshoot during saturation increase (Xiong, 2014). Water repellency, which may develop in long-term dry soils and reduce the soil infiltration capacity (and take some time to overcome), may be another explanation for these differences (Fig. 7a(2)) (Doerr et al., 2000). HYDRUS cannot simulate flow in repellent soils, which may result in simulation errors.

Second, detailed measurements of soil particle distributions and saturated hydraulic conductivities were also unavailable. Therefore, parameter optimization runs started with the average soil hydraulic parameters of different soil textures in this region (Table S1), which may significantly differ from the site-specific real values. On the other hand, the simultaneous fitting of 4 (single-porosity model) or up to 8 parameters (dual-porosity model) for each soil layer is likely to result in non-unique and local optimal parameter sets (Hopmans and Šimůnek, 1999). Global parameter optimization algorithms may help improve this aspect (Zhou et al., 2022). However, since a single HYDRUS model execution requires up to 50 seconds in this study, global optimization may face a very high computational cost. Alternatively, we can identify highly correlated parameters by correlation matrices (Figs. S10-S15) and fix some of them in future parameter optimization, thus alleviating the computational burden.

4.4 Suitability of implementing Ag-MAR

Because of their close proximity, the three profiles had the same land use and hydroclimatological conditions but differed in subsurface hydrogeology. This study can therefore provide some insights into the field-scale variability that one can expect when implementing Ag-MAR at the field scale.

While HS provided the largest recharge efficiency compared to MS and LS, recharge efficiency between sites varied only between 88% and 90%, because of similar effective saturated hydraulic conductivities at layers above 200 cm as discussed in Sections 3.3 and 3.4.

However, the degree of preferential flow varied distinctly between the three profiles, with HS showing the largest degree of preferential flow, and MS the least indication of preferential flow, and LS being in between the two (Fig. S11). Similarly, travel times (flow velocities) were longest (slowest) at MS, followed by LS, and were shortest (fastest) at HS (Table 6, Fig. 7c). Bromide transport velocities differed by as much as 119% between the three sites. This can also be verified by the dynamics in groundwater table depth and EC (Fig. S8). For example, there were abrupt decreases in groundwater depth and increases in EC after the beginning of flooding at LS and HS, which reached steady rates after a few days. In addition, the peaks in groundwater EC (about 2000 μS/cm at LS and 3500 μS/cm at HS) were much higher than pore water ECs in the bottom part (about 300~500 cm) of the soil profiles before flooding (about 1450~1650 μS/cm at LS, and 1050 μS/cm at HS (Fig. S5d, Fig. S7d). This suggests that preferential flow transported salts from the soil surface layers (with much higher pore-water ECs) to groundwater while bypassing the soil matrix in the upper parts of the soil profiles. In contrast, the groundwater table rise and EC dynamics were always more subtle at MS, representing a slower flow rate in the form of piston flow. The occurrence of preferential flow helps accelerate the timing of soil salt leaching at HS and LS, but also poses a greater risk for microbes or contaminants to be transported to groundwater since it reduces the time available for chemical or pathogen immobilization or degradation (Willkommen et al., 2021). However, evaluating the amount of a non-conservative pollutant transported to groundwater because of preferential flow needs further modeling studies.

Overall, all three profiles were able to achieve similar groundwater recharge efficiencies under the tested flooding regime for Ag-MAR (Table 1) considering their varying soil textures (Fig. 2). However, the water flow and solute transport processes might be very distinct. The suitability of implementing Ag-MAR depends on specific needs. In practical applications, the vadose zone with higher sand contents (such as HS) may imply more preferential flow (Sendros et al., 2020), which promotes more focused soil salt leaching, while a vadose zone with more silt contents (such as MS) would likely have a more muted contaminant transport response.

5 Conclusions

Our modeling results show that the dual-porosity models (considering preferential flow) can better fit the arrival times of bromide fronts but cannot significantly improve the overall model performance. Preferential flow occurred due to the combined effects of dry antecedent soil moisture followed by flooding, dry climate, soil texture, and the incorporation of almond wood chips into the topsoil, etc.

Preferential flow did not significantly impact the water balance calculations (within 2%), but it decreased the travel times of bromide from the soil surface to different depths of the soil profiles by up to 38%, compared to the predictions provided by the single-porosity model.

In terms of groundwater recharge potential, HS showed a higher efficiency than MS or LS, but the differences were relatively minor (within 2%). LS showed the highest degree of preferential flow, followed by HS and MS, and the overall average bromide transport velocities differed by up to 119%. In brief, similar recharge efficiency can be achieved at sites with differing soil texture profiles but subsurface heterogeneity can have substantial effects on salt and contaminant transport dynamics, which should be considered when implementing Ag-MAR.

The potential occurrence of lateral interflow is another important reason behind the model deficiency and may lead to errors in the water balance calculation in our relatively small experimental plots. In addition, we focused mainly on the effects of soil textural differences (i.e., between-lithofacies or large-scale heterogeneity) on Ag-MAR recharge and neglected the impact of horizontal heterogeneities within lithofacies (small-scale heterogeneity). Future work should extend the current 1D modeling analysis to 2D/3D to get full insight into soil heterogeneity's impacts (especially within-lithofacies or small-scale heterogeneity) on Ag-MAR recharge.

Acknowledgment

This research was supported by the Gordon and Betty Moore Foundation (grant no. 7975), the USDA National Institute of Food and Agriculture (grant no. CA-D-LAW-2513-H), USDA National Institute of Food and Agriculture (grant no. 2021-68012-35914), and USDA Natural Resources Conservation Agreement NR183A750023C005. We also acknowledge the editors and two anonymous reviewers for their constructive comments on this manuscript.

References

Alam, S., Borthakur, A., Ravi, S., Gebremichael, M., and Mohanty, S.K., (2021), Managed aquifer recharge implementation criteria to achieve water sustainability. *Science of the Total Environment*, *768*, pp. 19, doi:10.1016/j.scitotenv.2021.144992

Arnaud, E., Best, A., Parker, B.L., Aravena, R., and Dunfield, K., (2015), Transport of Escherichia coli through a thick vadose Zone. *J. Environ. Qual.*, *44*(5), pp. 1424-1434, doi:10.2134/jeq2015.02.0067

Bachand, P.A.M., Roy, S.B., Choperena, J., Cameron, D., and Horwath, W.R., (2014), Implications of using on-farm flood flow capture to recharge groundwater and mitigate flood risks along the Kings River, CA. *Environ. Sci. Technol.*, *48*(23), pp. 13601-13609, doi:10.1021/es501115c

Bali, K.M., Mohamed, A.Z., Begna, S., Wang, D., Putnam, D., Dahlke, H.E., and Eltarabily, M.G., (2023), The use of HYDRUS-2D to simulate intermittent Agricultural Managed Aquifer Recharge (Ag-MAR) in Alfalfa in the San Joaquin Valley. *Agricultural Water Management*, *282*, pp. 15, doi:10.1016/j.agwat.2023.108296

Botros, F.E., Onsoy, Y.S., Ginn, T.R., and Harter, T., (2012), Richards Equation-Based Modeling to Estimate Flow and Nitrate Transport in a Deep Alluvial Vadose Zone. *Vadose Zone Journal*, *11*(4), pp. 16, doi:10.2136/vzj2011.0145

Bradford, S.A., Leij, F.J., Schijven, J., and Torkzaban, S., (2017), Critical role of preferential flow in field-scale pathogen transport and retention. *Vadose Zone Journal*, *16*(4), pp. 13, doi:10.2136/vzj2016.12.0127

Chen, C.C., Roseberg, R.J., and Selker, J.S., (2002), Using microsprinkler irrigation to reduce leaching in a shrink/swell clay soil. *Agricultural Water Management*, *54*(2), pp. 159-171, doi:10.1016/s0378-3774(01)00150-0

Clapp, R.B., and Hornberger, G.M., (1978), Empirical equations for some soil hydraulic-properties. *Water Resources Research*, *14*(4), pp. 601-604, doi:10.1029/WR014i004p00601

Council, N.R., Conceptual models of flow and transport in the fractured vadose zone, National Academies Press, pp., 2001.

Dahlke, H.E., LaHue, G.T., Mautner, M.R., Murphy, N.P., Patterson, N.K., Waterhouse, H., Yang, F., and Foglia, L., Managed aquifer recharge as a tool to enhance sustainable groundwater management in California: examples from field and modeling studies, In Advances in chemical pollution, environmental management and protection, Elsevier, pp. 215-275, 2018.

de Vries, J.J., and Simmers, I., (2002), Groundwater recharge: an overview of processes and challenges. *Hydrogeology Journal*, *10*(1), pp. 5-17, doi:10.1007/s10040-001-0171-7

Doerr, S.H., Shakesby, R.A., and Walsh, R.P.D., (2000), Soil water repellency: its causes, characteristics and hydro-geomorphological significance. *Earth-Sci. Rev.*, *51*(1-4), pp. 33-65, doi:10.1016/s0012-8252(00)00011-8

Ganot, Y., and Dahlke, H.E., (2021), A model for estimating Ag-MAR flooding duration based on crop tolerance, root depth, and soil texture data. *Agricultural Water Management*, *255*, pp. 12, doi:10.1016/j.agwat.2021.107031

Gelhar, L.W., Welty, C., and Rehfeldt, K.R., (1992), A CRITICAL-REVIEW OF DATA ON FIELD-SCALE DISPERSION IN AQUIFERS. *Water Resources Research*, *28*(7), pp. 1955-1974, doi:10.1029/92wr00607

Gerke, H.H., and van Genuchten, M.T., (1993), Evaluation of a 1st-order water transfer term for variably saturated dual-porosity flow models. *Water Resources Research*, *29*(4), pp. 1225-1238, doi:10.1029/92wr02467

Guo, Z., Fogg, G.E., Chen, K., Pauloo, R., and Zheng, C., (2023), Sustainability of regional groundwater quality in response to managed aquifer recharge. *Water Resources Research*, *59*(1), pp. e2021WR031459,

Gurevich, H., Baram, S., and Harter, T., (2021), Measuring nitrate leaching across the critical zone at the field to farm scale. *Vadose Zone Journal*, *20*(2), pp. 16, doi:10.1002/vzj2.20094

Harter, T., and Yeh, T.C.J., (1996), Conditional stochastic analysis of solute transport in heterogeneous, variably saturated soils. *Water Resources Research*, *32*(6), pp. 1597-1609, doi:10.1029/96wr00503

Haws, N.W., Rao, P.S.C., Šimůnek, J., and Poyer, I.C., (2005), Single-porosity and dual-porosity modeling of water flow and solute transport in subsurface-drained fields using effective field-scale parameters. *Journal of Hydrology*, *313*(3-4), pp. 257-273, doi:10.1016/j.jhydrol.2005.03.035

Ho, C.K., and Webb, S.W., (1998), Capillary barrier performance in heterogeneous porous media. *Water Resources Research*, *34*(4), pp. 603-609, doi:10.1029/98wr00217

Hopmans, J., and Šimůnek, J., Review of inverse estimation of soil hydraulic properties, in van Genuchten, M. Th., F. J. Leij, and L. Wu (eds.), *Characterization and Measurement of the Hydraulic Properties of Unsaturated Porous Media*, University of California, Riverside, CA, pp. 643-659, 1999.

Imig, A., Augustin, L., Groh, J., Putz, T., Elsner, M., Einsiedl, F., and Rein, A., (2023), Fate of herbicides in cropped lysimeters: 2. Leaching of four maize herbicides considering different processes. *Vadose Zone Journal*, *22*(5), pp. 14, doi:10.1002/vzj2.20275

Isch, A., Montenach, D., Hammel, F., Ackerer, P., and Coquet, Y., (2019), A Comparative Study of Water and Bromide Transport in a Bare Loam Soil Using Lysimeters and Field Plots. *Water*, *11*(6), pp. 25, doi:10.3390/w11061199

Jiang, S., Pang, L.P., Buchan, G.D., Šimůnek, J., Noonan, M.J., and Close, M.E., (2010), Modeling water flow and bacterial transport in undisturbed lysimeters under irrigations of dairy shed effluent and water using HYDRUS-1D. *Water Res.*, *44*(4), pp. 1050-1061, doi:10.1016/j.watres.2009.08.039

Kocis, T.N., and Dahlke, H.E., (2017), Availability of high-magnitude streamflow for groundwater banking in the Central Valley, California. *Environmental Research Letters*, *12*(8), pp. 13, doi:10.1088/1748-9326/aa7b1b

Köhne, J.M., Köhne, S., Mohanty, B.P., and Šimůnek, J., (2004), Inverse mobile-immobile modeling of transport during transient flow: Effects of between-domain transfer and initial water content. *Vadose Zone Journal*, *3*(4), pp. 1309-1321, doi:10.2113/3.4.1309

Kourakos, G., Dahlke, H.E., and Harter, T., (2019), Increasing Groundwater Availability and Seasonal Base Flow Through Agricultural Managed Aquifer Recharge in an Irrigated Basin. *Water Resources Research*, *55*(9), pp. 7464-7492, doi:10.1029/2018wr024019

Levintal, E., Huang, L., García, C.P., Coyotl, A., Fidelibus, M.W., Horwath, W.R., Rodrigues, J.L.M., and Dahlke, H.E., (2023a), Nitrogen fate during agricultural managed aquifer recharge: Linking plant response, hydrologic, and geochemical processes. *Science of the Total Environment*, *864*, pp. 161206,

Levintal, E., Kniffin, M.L., Ganot, Y., Marwaha, N., Murphy, N.P., and Dahlke, H.E., (2023b), Agricultural managed aquifer recharge (Ag-MAR)-a method for sustainable groundwater management: A review. *Crit. Rev. Environ. Sci. Technol.*, *53*(3), pp. 291-314, doi:10.1080/10643389.2022.2050160

Li, E., Shanholtz, V., and Carson, E., (1976), Estimating saturated hydraulic conductivity and capillary potential at the wetting front, Dep. of Agr. Eng. *Va. Polytech. Inst. and State Univ., Blacksburg*,

Marwaha, N., Kourakos, G., Levintal, E., and Dahlke, H.E., (2021), Identifying Agricultural Managed Aquifer Recharge Locations to Benefit Drinking Water Supply in Rural Communities. *Water Resources Research*, *57*(3), pp. 24, doi:10.1029/2020wr028811

Mitchell, A.R., Ellsworth, T.R., and Meek, B.D., (1995), Effect of root systems on preferential flow in swelling soil. *Commun. Soil Sci. Plant Anal.*, *26*(15-16), pp. 2655-2666, doi:10.1080/00103629509369475

Mitchell, A.R., and van Genuchten, M.T., (1993), Flood irrigation of a cracked soil. *Soil Science Society of America Journal*, *57*(2), pp. 490-497, doi:10.2136/sssaj1993.03615995005700020032x

Mualem, Y., (1976), A new model for predicting the hydraulic conductivity of unsaturated porous media. *Water Resources Research*, *12*(3), pp. 513-522, doi:10.1029/WR012i003p00513

Murphy, N.P., Waterhouse, H., and Dahlke, H.E., (2021), Influence of agricultural managed aquifer recharge on nitrate transport: The role of soil texture and flooding frequency. *Vadose Zone Journal*, *20*(5), pp. 16, doi:10.1002/vzj2.20150

Nimmo, J.R., Perkins, K.S., Plampin, M.R., Walvoord, M.A., Ebel, B.A., and Mirus, B.B., (2021), Rapid-response unsaturated zone hydrology: Small-scale data, small-scale theory, big problems. *Front. Earth Sci.*, *9*, pp. 7, doi:10.3389/feart.2021.613564

Perzan, Z., Osterman, G., and Maher, K., (2023), Controls on flood managed aquifer recharge through a heterogeneous vadose zone: hydrologic modeling at a site characterized with surface geophysics. *Hydrology and Earth System Sciences*, *27*(5), pp. 969-990, doi:10.5194/hess-27-969-2023

Radcliffe, D.E., and Šimůnek, J., Soil physics with HYDRUS: Modeling and applications, CRC Press, pp., 2018.

Sasidharan, S., Bradford, S.A., Šimůnek, J., and Kraemer, S.R., (2021), Virus transport from drywells under constant head conditions: A modeling study. *Water Res.*, *197*, pp. 14, doi:10.1016/j.watres.2021.117040

Scanlon, B.R., Faunt, C.C., Longuevergne, L., Reedy, R.C., Alley, W.M., McGuire, V.L., and McMahon, P.B., (2012), Groundwater depletion and sustainability of irrigation in the US High Plains and Central Valley. *Proc. Natl. Acad. Sci. U. S. A.*, *109*(24), pp. 9320-9325, doi:10.1073/pnas.1200311109

Selker, J., Cao, W.D., and Roseberg, R., Use of ultra-low rate application devices to eliminate macropore flow during irrigation, *5th International Microirrigation Congress - Microirrigation for a Changing World: Conserving Resources/Preserving the Environment*, 95, Amer Soc Agricultural Engineers, Orlando, Fl, pp. 54-59, 1995.

Sendros, A., Himi, M., Lovera, R., Rivero, L., Garcia-Artigas, R., Urruela, A., and Casas, A., (2020), Electrical resistivity tomography monitoring of two managed aquifer recharge ponds in the alluvial aquifer of the Llobregat River (Barcelona, Spain). *Near Surf. Geophys.*, *18*(4), pp. 353-368, doi:10.1002/nsg.12113

Si, B., Dyck, M., and Parkin, G.W., (2011), Flow and Transport in Layered Soils PREFACE. *Can. J. Soil Sci.*, *91*(2), pp. 127-132, doi:10.4141/cjss11501

Siebert, S., Burke, J., Faures, J.M., Frenken, K., Hoogeveen, J., Doll, P., and Portmann, F.T., (2010), Groundwater use for irrigation - a global inventory. *Hydrology and Earth System Sciences*, *14*(10), pp. 1863-1880, doi:10.5194/hess-14-1863-2010

Šimůnek, J., and Hopmans, J.W., (2002), 1.7 parameter optimization and nonlinear fitting. *Methods of Soil Analysis: Part 4 Physical Methods*, *5*, pp. 139-157,

Šimůnek, J., Jarvis, N.J., van Genuchten, M.T., and Gardenas, A., (2003), Review and comparison of models for describing non-equilibrium and preferential flow and transport in the vadose zone. *Journal of Hydrology*, *272*(1-4), pp. 14-35,

Šimůnek, J., and van Genuchten, M.T., (2008), Modeling nonequilibrium flow and transport processes using HYDRUS. *Vadose Zone Journal*, *7*(2), pp. 782-797, doi:10.2136/vzj2007.0074

Šimůnek, J., van Genuchten, M.T., and Sejna, M., (2016), Recent developments and applications of the HYDRUS computer software packages. *Vadose Zone Journal*, *15*(7), pp. 25, doi:10.2136/vzj2016.04.0033

Šimůnek, J., Wendroth, O., Wypler, N., and van Genuchten, M.T., (2001), Non-equilibrium water flow characterized by means of upward infiltration experiments. *Eur. J. Soil Sci.*, *52*(1), pp. 13-24, doi:10.1046/j.1365-2389.2001.00361.x

Sprenger, C., Hartog, N., Hernandez, M., Vilanova, E., Grutzmacher, G., Scheibler, F., and Hannappel, S., (2017), Inventory of managed aquifer recharge sites in Europe: historical development, current situation and perspectives. *Hydrogeology Journal*, *25*(6), pp. 1909-1922, doi:10.1007/s10040-017-1554-8

van Genuchten, M.T., (1980), A closed-form equation for predicting the hydraulic conductivity of unsaturated soils. *Soil Science Society of America Journal*, *44*(5), pp. 892-898, doi:10.2136/sssaj1980.03615995004400050002x

Wang, C.Z., Liu, G., McNew, C.P., Volkmann, T.H.M., Pangle, L., Troch, P.A., Lyon, S.W., Kim, M., Huo, Z.L., and Dahlke, H.E., (2022), Simulation of experimental synthetic DNA tracer transport through the vadose zone. *Water Res.*, *223*, pp. 10, doi:10.1016/j.watres.2022.119009

Wang, C.Z., Wang, R.Y., Huo, Z.L., Xie, E., and Dahlke, H.E., (2020), Colloid transport through soil and other porous media under transient flow conditions-A review. *Wiley Interdisciplinary Reviews-Water*, *7*(4), pp. 33, doi:10.1002/wat2.1439

Wang, Y.C., Li, Y., Wang, X.F., and Chau, H.W., (2018), Finger flow development in layered water-repellent soils. *Vadose Zone Journal*, *17*(1), pp. 11, doi:10.2136/vzj2017.09.0171

Waterhouse, H., Bachand, S., Mountjoy, D., Choperena, J., Bachand, P.A.M., Dahlke, H.E., and Horwath, W.R., (2020), Agricultural managed aquifer recharge - water quality factors to consider. *Calif. Agric.*, *74*(3), pp. 144-154, doi:10.3733/ca.2020a0020

Wendt, D.E., Van Loon, A.F., Scanlon, B.R., and Hannah, D.M., (2021), Managed aquifer recharge as a drought mitigation strategy in heavily-stressed aquifers. *Environmental Research Letters*, *16*(1), pp. 13, doi:10.1088/1748-9326/abcfe1

Willkommen, S., Lange, J., Ulrich, U., Pfannerstill, M., and Fohrer, N., (2021), Field insights into leaching and transformation of pesticides and fluorescent tracers in agricultural soil. *Science of the Total Environment*, *751*, pp. 12, doi:10.1016/j.scitotenv.2020.141658

WWDR, (2022), Groundwater: Making the invisible visible. *The United Nations World Water Development Report*,

Xiong, Y.W., (2014), Flow of water in porous media with saturation overshoot: A review. *Journal of Hydrology*, *510*, pp. 353-362, doi:10.1016/j.jhydrol.2013.12.043

Zhou, T., Šimůnek, J., and Braud, I., (2021), Adapting HYDRUS-1D to simulate the transport of soil water isotopes with evaporation fractionation. *Environ. Modell. Softw.*, *143*, pp. 105118, doi:https://doi.org/10.1016/j.envsoft.2021.105118

Zhou, T., Šimůnek, J., Braud, I., Nasta, P., Brunetti, G., and Liu, Y., (2022), The impact of evaporation fractionation on the inverse estimation of soil hydraulic and isotope transport parameters. *Journal of Hydrology*, *612*, pp. 128100, doi:https://doi.org/10.1016/j.jhydrol.2022.128100

Zhou, T., Šimůnek, J., Nasta, P., Brunetti, G., Gaj, M., Neukum, C., and Post, V., (2023), The Impact of Soil Tension on Isotope Fractionation, Transport, and Interpretations of the Root Water Uptake Origin. *Water Resources Research*, *59*, pp. e2022WR034023, doi:https://doi.org/10.1029/2022WR034023